

A localized waveform inversion at teleseismic distances: an application to the D'' region beneath the Cocos plate

Yang He, Alan Levander and Fenglin Niu

Department of Earth science, Rice University, 6100 Main Street, Houston, TX 77005. E-mail: niu@rice.edu

Accepted 2009 December 17. Received 2009 December 17; in original form 2009 April 28

SUMMARY

A localized waveform inversion technique based on hybrid modelling was developed to investigate shear wave velocity structure of the lowermost mantle. Utilizing ray theory and the Kirchhoff integral, the source wavefield from hypocentre and the receiver wavefield recorded at Earth's surface was extrapolated to the subsurface near the core–mantle boundary (CMB). Ray theory solutions are interfaced with the finite difference displacements computed in a local heterogeneous region near the CMB. The velocity structure is updated iteratively by zero-lag cross-correlation of the forward and backward wavefields in region where the finite-difference displacements were computed. As the finite difference method is applied in a small region only, the hybrid method takes much less computer memory when it is implemented to invert localized structures. We applied this method to the broadband waveform data recorded by RISTRA array from a deep south American earthquake. The resulting depth and velocity contrast across the D'' discontinuity agree reasonably well with previous observations, suggesting that the hybrid waveform inversion is a feasible and an effective technique for imaging the heterogeneous D'' region.

Key words: Body waves; Seismic tomography; Wave propagation.

1 INTRODUCTION

The lowermost several hundred kilometres of the Earth's mantle (the D'' layer) above the core–mantle boundary (CMB) is known to be very heterogeneous in terms of seismic structure. D'' heterogeneities cover a wide range of scales that vary from a few kilometres to a few thousands of kilometres laterally and tenths to tens of per cent in intensity (e.g. Garnero *et al.* 1993; Mori & Helmberger 1995; Revenaugh & Meyer 1997; Vidale & Hedlin 1998; Wen & Helmberger 1998; Ishii & Tromp 1999; Niu & Wen 2001; Wen *et al.* 2001; Grand 2002; Sun *et al.* 2006; van der Hilst *et al.* 2007). In some regions, the layer is upper-bounded by a sharp discontinuity (the D'' discontinuity, Lay & Helmberger 1983), which is characterized by a large increase in S-wave velocity but not in P-wave velocity (e.g. Lay & Garnero 2004). It also appears that the depth and velocity contrast of the D'' discontinuity change rapidly and drastically with locations. In addition to these large variations in the D'' discontinuity structure, many other seismic inhomogeneities, such as strong small-scale scatterers and ultralow-velocity zones, are also revealed by numerous seismic studies (e.g. Garnero *et al.* 1993; Vidale & Hedlin 1998; Wen & Helmberger 1998; Niu & Wen 2001; Miller & Niu 2008). Determining the geometry and amplitude of these complicated seismic structures thus becomes very challenging, although it is crucial in constraining the origin of these anomalies and important in understanding the Earth's deep dynamics.

A number of seismic techniques has been developed and employed to study seismic structures of the D'' layer. For example,

precursors to the compressional waves that traverse through the Earth's core at the distance range of 130°–143° have been frequently studied to image small-scale heterogeneities or scatterers in the lowermost mantle (e.g. Vidale & Hedlin 1998; Niu & Wen 2001; Miller & Niu 2008). Forward modelling of the waveform triplication observed between 70° and 85° is a classic approach and has been very successful in mapping the D'' discontinuity (e.g. Kendall & Nangini 1996; also see Wysession *et al.* 1998, for a review). Most early studies employed modelling techniques developed for 1-D structure, which sometime are not suitable if the D'' region has large 3-D anomalies. It is unclear how 3-D structures could affect those localized 1-D models.

The staggered grid finite-difference (FD) method (Virieux 1984; Levander 1988) is one of the most useful numerical methods to simulate wave propagation in heterogeneous media. Direct application of the FD method to teleseismic modelling at large distances is, however, always hindered by the intrinsic numerical dispersion in the method as well as the massive computational costs. Wen (2002) proposed a hybrid 2-D method that combines analytic and numerical solutions of the wave equation for computing synthetic seismograms at large distances. The numerical approach is applied only to a targeted localized region with large lateral heterogeneities. More recently, with enhanced computer powers Thorne *et al.* (2007) implemented a 2.5-D FD method to a 2-D model extending from Earth's surface to the CMB and used it to investigate the D'' region beneath the Cocos plate. In general, forward modelling is mostly used and best suitable for small data sets of good

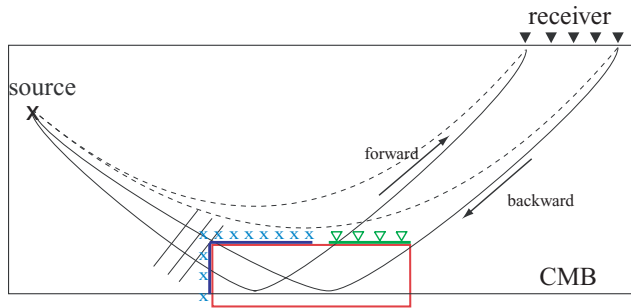


Figure 1. Schematic illustration of the hybrid method. Strong heterogeneities are confined with the red box where the finite-difference technique is applied. X and solid reverse triangles indicate the source and the receivers, respectively. The virtual sources and virtual receivers are indicated by blue crosses and green open triangles, respectively. Arrows indicate the forward and backward extrapolations between the wavefields at different depth levels. The top left-hand boundary shown in blue indicates the region S (see text).

quality due to the large amount of manual labour involved in iterating models.

Recent developments in passive seismic observations make it possible to apply imaging techniques developed for petroleum exploration, such as waveform stacking, migration and inversion to investigate deep mantle structures. Thomas *et al.* (2004) applied a 1-D diffraction migration technique to the array data recorded in California from deep earthquakes occurring in South America to map the lateral variations of the D'' discontinuity beneath Central America. Hutko *et al.* (2006) applied a Kirchhoff migration to a data set with similar ray geometry of Thomas *et al.* (2004). Both studies suggest the D'' discontinuity beneath the Cocos Plate has a 100-km vertical step occurring of a lateral transition of less than 100 km. Wang *et al.* (2006) inverted the ScS wavefield using a generalized Radon transform scheme (GRT, Beylkin & Burridge 1990). The inverted 3-D volume revealed a very complicated picture of the lowermost mantle beneath the Americas, filled with reflectors at various depth levels.

The issue of seismic inversion/imaging can be generalized to find the velocity perturbation field that provides the best explanation for seismic data. Theoretically, migration is the first iteration in the inversion process, not the exact solution of the perturbation field. Waveform inversion, however, seeks to find the true perturbation field by directly solving the partial differential wave equations. When the wavefield is densely sampled, waveform inversion has been proven to be able to image subwavelength scale structure (Pratt *et al.* 1998). Here we describe a localized 2-D waveform inversion scheme designed for imaging the D'' layer with a reflection source–receiver geometry. We used a hybrid method similar to Wen (2002) for computing synthetic seismogram. The inversion is implemented with virtual sources and receivers located around a 2-D box centred at the ScS reflection points on the CMB (Fig. 1). Our main goal is to investigate the feasibility of the method in imaging reflectors and scatterers with various length scales with synthetic data. A calibration study with the SH waveform data recorded by a large-scale linear array yield velocity structure consistent with previous interpretations.

2 HYBRID FORWARD MODELLING

The concept of using hybrid method to compute synthetic seismograms at teleseismic distances is well described in Wen (2002). As

our main effort is the implementation of waveform inversion, we only briefly review the method here. As shown in Fig. 1, the SH wavefield is computed differently along its propagation path. Inside the 2-D box where strong heterogeneities exist we calculated the wavefield numerically with a FD method, whereas outside the box we used ray theory to approximate the SH wave propagation. We employed the velocity–stress staggered-grid scheme (Virieux 1984; Levander 1988) and used FD operator, which is fourth-order in space and second-order in time. Interfacing the finite difference scheme with the ray solution is analogous to the source insertion method described in Alterman & Karal (1968). The source wave field is added along the top and left boundary of the FD region (Fig. 1). The FD calculation in this source region (hereafter region S) is slightly different from the rest (hereafter FD region). In the FD region, the full wave field is calculated with continuously updated sources from the S region. Only the reflection field from the underlying heterogeneous FD region is computed for the S region. Around the grid periphery, we used the perfectly matched layer (PML) method (Berenger 1994) as an absorbing boundary condition to eliminate artificial reflections from the two sides of the box.

It is well known that one can use the Kirchhoff integral to compute the wavefield from one depth level to another depth level. Thus once the wavefield at the top of the FD box is computed, we used the following Rayleigh II integral (Berkhout & Wapenaar 1988) in the extrapolating the wavefield to the surface

$$U_A = -\frac{1}{2\pi} \int_S U_s \frac{\partial G}{\partial n} dS. \quad (1)$$

Here U_s is the velocity/displacement field output from the FD calculation and G is the Green's function calculated based on ray theory. The integration is along a straight line along the top of the FD box. Similarly, we can back project the velocity/displacement field recorded at surface to any position in the subsurface using the same integral (Wapenaar *et al.* 1989)

$$U_S = -\frac{1}{2\pi} \int_S U_A \frac{\partial G^*}{\partial n} dS. \quad (2)$$

Here G^* is the complex conjugate of the Green's function, G , which is a time reversal operator. U_A and U_S are the surface and subsurface velocity/displacement fields, respectively. With this forward and backward propagation, the waveform inversion can be simplified to waveform tomography for a reflection geometry with an appropriately curved wavefront from the earthquake which is input as a source to a region at the CMB defined on rectangular grids.

The hybrid forward modelling developed here was first benchmarked with reflectivity synthetics (Kennett 1988). The model used in the calculation is a modification of the iasp91 model (Kennett & Engdahl 1991) in which we have introduced a sharp D'' discontinuity and a faster-than-normal D'' layer based on the model of Sun *et al.* (2006) (Fig. 2a). Figs 2(b)–(e) showed four snapshots of the wavefield propagating through the D'' region. Note the clear reflections from the CMB (ScS) and the D'' discontinuity (SdS). The displacement fields at 2400 km depth and the Earth's surface are shown in Figs 3(a) and (b), respectively. A Gaussian wavelet was used as source time function in the calculation. Note that the amplitude of the SdS phase increases with distance and the SdS phase finally merges with the ScS arrival. A line source is intrinsically assumed in the 2-D synthetic calculation. We used the conversion equation of

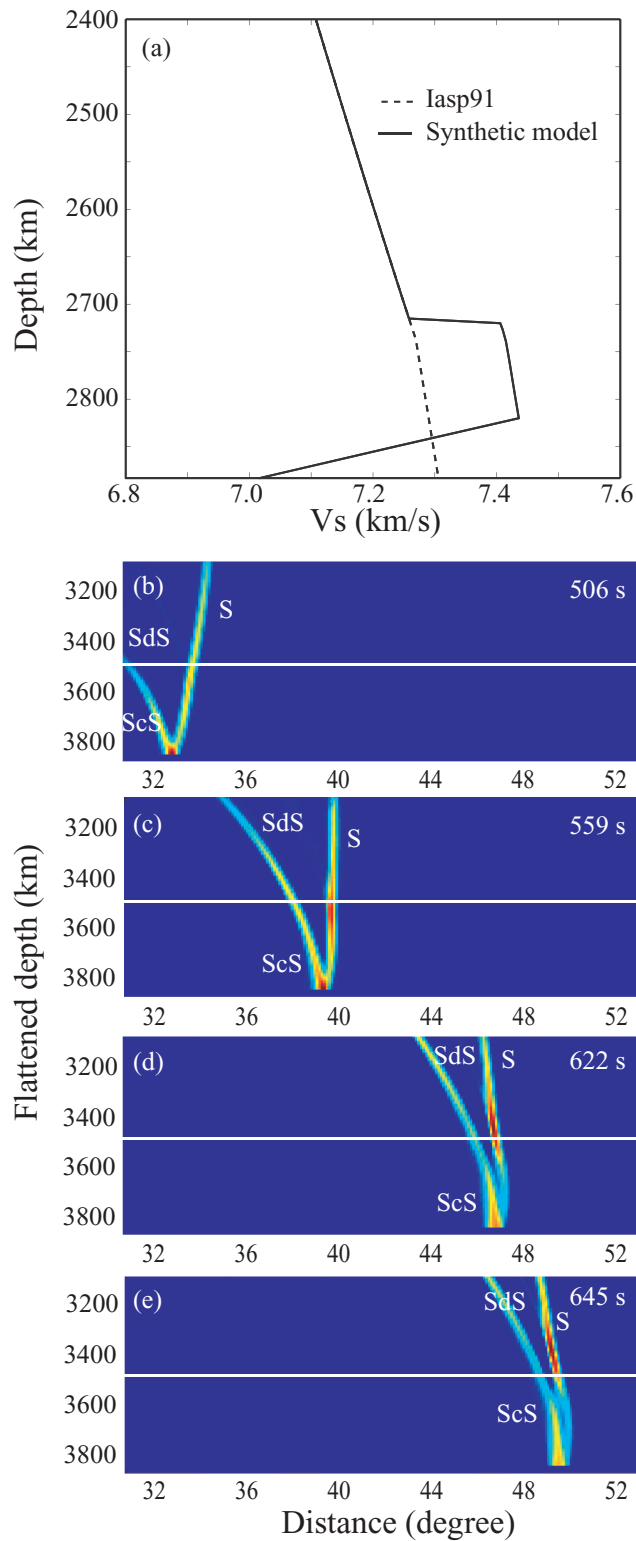


Figure 2. (a) The 1-D model used in the calibration test (solid line) is shown together with the iasp91 velocity model (dashed line). The model, based on the work of Sun *et al.* 2006, has an elevated S -wave velocity in the depth range of 2720–2840 km and a reduced velocity layer right above the CMB. (b–e) Snapshots of SH wavefield as the SH wave propagates through the revised iasp91 model shown in (a). The white line indicates the location of the D' discontinuity and depths are after the earth-flattening transformation. Note the strong reflection from the D' between the S and ScS wavefields.

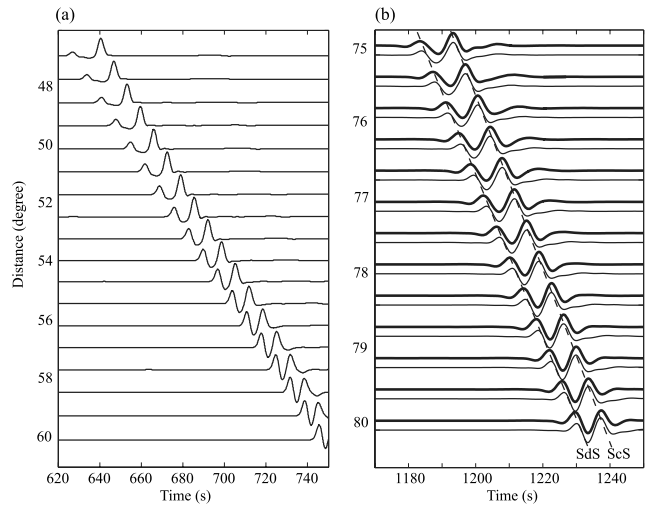


Figure 3. (a) Synthetic seismograms recorded at virtual receivers at the depth of 2400 km. (b) Synthetic seismograms at the surface (thick lines) calculated using the hybrid method are shown together with reflectivity synthetics (thin lines). The revised iasp91 model shown in Fig. 2(a) is used in computing the synthetics. Note the gradual increase of SdS amplitude with increasing epicentral distance.

Stead & Helmberger (1988)

$$U_{\text{point}} = \frac{2}{\sqrt{R+\sqrt{x}}} \frac{1}{\sqrt{t}} * \frac{d}{dt} U_{\text{line}}, \quad (3)$$

to compute the point source response. Here R and x are the total and horizontal distances, respectively.

3 LOCALIZED WAVEFORM INVERSION

In this section, we formulate the adjoint solution of the non-linear seismic waveform inversion problem (e.g. Tarantola 1984; Mora 1987; Pratt *et al.* 1998). Our data are the surface records, d , the model parameters are the shear modulus, μ and the corresponding synthetics are u . The residual error for model μ is defined as the difference between the synthetics and the observed data

$$\Delta d = u(\mu) - d_{\text{obs}}. \quad (4)$$

Here we seek to minimize the l_2 norm of the data residuals. The objective function is thus defined as

$$E(\mu) = \frac{1}{2} \|\Delta d\|^2. \quad (5)$$

The model parameters are updated in the direction that reduces the objective function

$$\mu^{n+1} = \mu^n - \alpha^n \nabla E^n. \quad (6)$$

Here n is iteration number and α is the step length, and $\nabla E(\mu)$ is the gradient of the objective function with respect to the model parameter, which can be represented as

$$\nabla E(\mu) = \frac{\partial u(\mu)}{\partial \mu}. \Delta d = J \cdot \Delta d. \quad (7)$$

Here $\frac{\partial u}{\partial \mu}$ is an important derivative, called Frechet derivative. It represents how the perturbation of model parameter μ has an effect on the synthetic data u . It can be computed by taking derivative of the wave equation with respect to μ_j .

The SH wave equation is

$$\frac{\partial}{\partial x} \left(\mu \frac{\partial u}{\partial x} \right) + \frac{\partial}{\partial z} \left(\mu \frac{\partial u}{\partial z} \right) + \rho \omega^2 u = f \quad (8)$$

or in a compact form

$$S \cdot u = f.$$

Taking derivative to get

$$\frac{\partial S}{\partial \mu_j} \cdot u_i + S \cdot \frac{\partial u_i}{\partial \mu_j} = 0. \quad (9)$$

Rearranging it, then

$$\frac{\partial u_i}{\partial \mu_j} \cdot = -S^{-1} \cdot \frac{\partial S}{\partial \mu_j} \cdot u_i. \quad (10)$$

Actually

$$\frac{\partial u_i}{\partial \mu_j} = -S^{-1} \cdot \nabla^2 u_i. \quad (11)$$

Inserting it into the gradient

$$\begin{aligned} \nabla E(\mu) &= \frac{\partial u_i(\mu)}{\partial \mu_j} \cdot \Delta d = -S^{-1} \cdot \nabla^2 u \cdot \Delta d \\ &= -S^{-1} \cdot (\nabla \cdot \nabla u) \cdot \Delta d. \end{aligned} \quad (12)$$

Transform it into time domain and S^{-1} is simply the Green's function, replaced by G .

$$\begin{aligned} \nabla E(\mu) &= - \int_{\mathbb{V}} G * (\nabla \cdot \nabla u) \Delta d \\ &= \int_{\mathbb{V}} \nabla G * \nabla u \Delta d - \int_{\mathbb{V}} \nabla \cdot (G * \nabla u) \Delta d. \end{aligned} \quad (13)$$

Here $\int_{\mathbb{V}} \nabla \cdot (G * \nabla u) \Delta d = \int_S (G * \nabla u) \Delta d$ can be written as an integral over the surface of the Earth, which vanishes because homogeneous boundary conditions are assumed according to the same steps as in Tarantola (1984). Thus

$$\nabla E(\mu) = \int_{\mathbb{V}} \nabla u * \nabla G \Delta d \quad (14)$$

by using result

$$\int dt f(t) * g(t) h(t) = \int dt f(-t) g(t) * h(-t) \quad (15)$$

we can get

$$\nabla E(\mu) = \int dt \sum_R \nabla u(-t) \nabla G * \Delta d(-t). \quad (16)$$

Here $\nabla G * \Delta d(-t)$ is the backpropagated wavefield in reverse time. R is the sum over receivers. We can see that the quantity used to update model parameters just represents the correlation between the forward propagated wavefield and backward propagated residual wavefield.

In general, waveform inversion can be performed in either the frequency or the time domain. Pratt *et al.* (1998) implemented waveform inversion in the space-frequency domain. Iteration is employed

at discrete frequencies, moving from low to high to mitigate the non-linearity of the inversion. By successively moving to higher frequencies of data and using results from the previous frequency as a starting model, higher frequency features of the model are included and give the solution character. Although the frequency domain method is efficient, it requires careful selection of frequencies and a significant amount of trial and error, which may affect the final result. Freudenreich & Shipp (2000) suggested that the time domain approach is more robust than the frequency domain approach. A time-domain inversion scheme was employed in this study.

4 APPLICATION TO SYNTHETIC DATA

We first applied the above inversion scheme to a synthetic data set to investigate its resolving power on reflectors and scatterers with various length scales in the D'' layer. A rectangular model with 286 by 1100 gridpoints is used in the synthetic test. Teleseismic SH waves usually have dominant frequencies lower than 0.5 Hz, corresponding to a wavelength of $\gtrsim 30$ km after applying a flattening transformation. The grid spacing is 3 km. The flattened iasp91 model is used as the background velocity model. With the above model parameters we can cover a region extending ~ 500 and ~ 3300 km in the vertical and horizontal directions, respectively. The input model (Fig. 4a) has four small-scale scatterers (15 km)

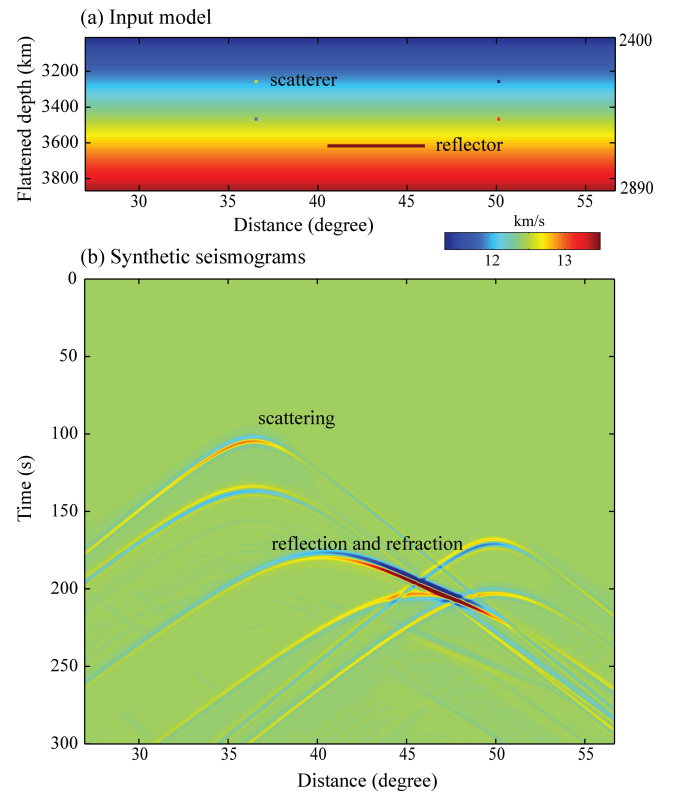


Figure 4. (a). The input model velocity model for the 2-D inversion test. Depths are after flattening transformation. The background velocity is iasp91, which is indicated by the uniform horizontal colours. The horizontal line represents a seismic reflector while the four dots indicate the isotropic scatterers, all with a 5 per cent positive or negative velocity fluctuation. See text for details on the geometry and amplitude of anomalies. (b) Synthetic seismograms recorded by virtual receivers at 2400 km depth calculated from a plane wave with an incident angle of 30° . The direct S arrival is muted in the display. Note the clear reflection and diffractions from the point scatterers.

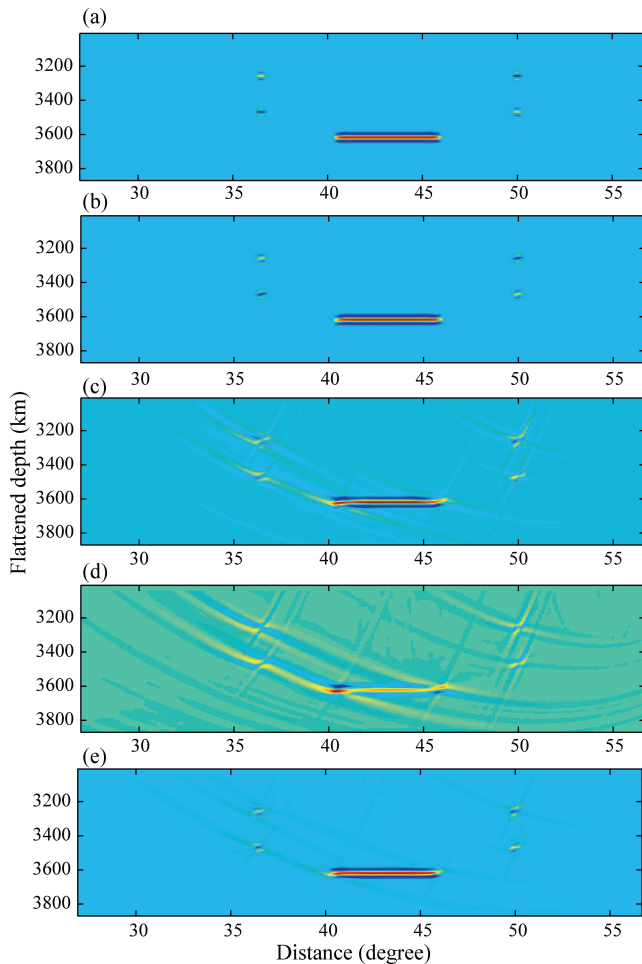


Figure 5. (a–d). The resulting 2-D velocity models from the localized inversion of the synthetic seismograms computed from a plane-wave source with an incident angle of 0° , 15° , 30° and 35° , respectively. (e) 2-D velocity model resulting from an inversion of the all the four data sets. Note the excellent agreement between these models are ~ 90 , ~ 80 , ~ 20 and ~ 10 per cent for the four plane-wave sources with an incidence angles of 0° , 15° , 30° and 35° , respectively.

and one large-scale reflector (15 km thick and 600 km in length), all with a 5 per cent velocity perturbation. The FD synthetic seismograms computed for a plane wave source with a 30° incident angle are shown in Fig. 4(b). Both the scattered and reflected wavefields can be clearly identified from the synthetics (Fig. 4b). We performed the waveform inversion with four sets of synthetic data corresponding four sources with incident angles of 0° , 15° , 30° and 35° , respectively. The resulting four models are shown in Fig. 5. The input velocity anomalies are well recovered in these images in terms of the position, polarity and amplitude of the anomalies. Smearing appears to increase rapidly with increasing incident angles. The result from an inversion of all the four data sets is shown in Fig. 5(e). It recovers the input model very well, suggesting that the localized inversion can resolve details of D'' velocity anomalies as if a data set covering a wide range of incidence angles, that is, contains sources at a range of epicentre distance. The same features were also observed in images computed from large incident angles (Fig. 6). A 50 km step was clearly imaged by seismic waves with intermediate incident angles (Figs 6a and b). At large incident angles with a post-critical geometry, the step is shown as a continuous structure

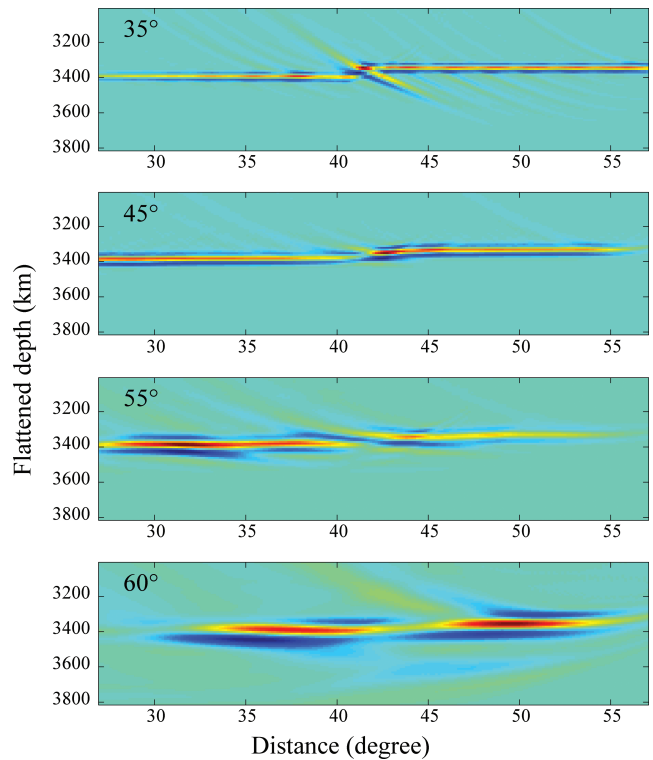


Figure 6. (a–d). The resulting 2-D images from the localized inversion of the synthetic seismograms computed from a plane-wave source with an incident angle of 35° , 45° , 55° and 60° , respectively. The input model has a D'' discontinuity with a 50 km step (in the flattened coordinate) in the middle. The step is recovered in all the images with different ray geometry although it becomes a continuous feature with large incident angles (c–d). A phase correction was applied to the synthetic data before the 2-D inversion (see text for details).

in the images (Figs 6c and d). The depth difference is, however, well resolved with the assumed ray geometry. The SdS waveform consists of a positive refraction and a post-critical reflection from the D'' discontinuity. To recover the correct polarity and depth of the discontinuity, it is necessary to account for the phase shift in post-critical reflection. The phase shift was determined when the cross correlation between S and SdS after the phase correction reaches its maximum.

5 APPLICATION TO RISTRA ARRAY DATA

As an example of the inversion method we have applied the inversion technique developed here to a passive data set recorded by the linear RISTRA Array (Wilson *et al.* 2005). The seismograms are recordings of a deep focus (608 km), M_w 6.9 earthquake occurring in northern Argentina on 2000 April 23 (origin time 9:27:23.3; epicentre: 28.31°S , 62.99°W , Fig. 7 inset). The NW-oriented RISTRA array consisted of 54 broad-band instruments covering about 950 km with an average station spacing of 18 km. The array is located at $\sim 70^\circ$ – 80° away from the earthquake, and the SzS reflection points sample the CMB region of 0° – 4° N and 275° – 278° E below the Cocos-Nazca plate boundary (red circles in Fig. 7), which lies at the southern end of probably the best-studied

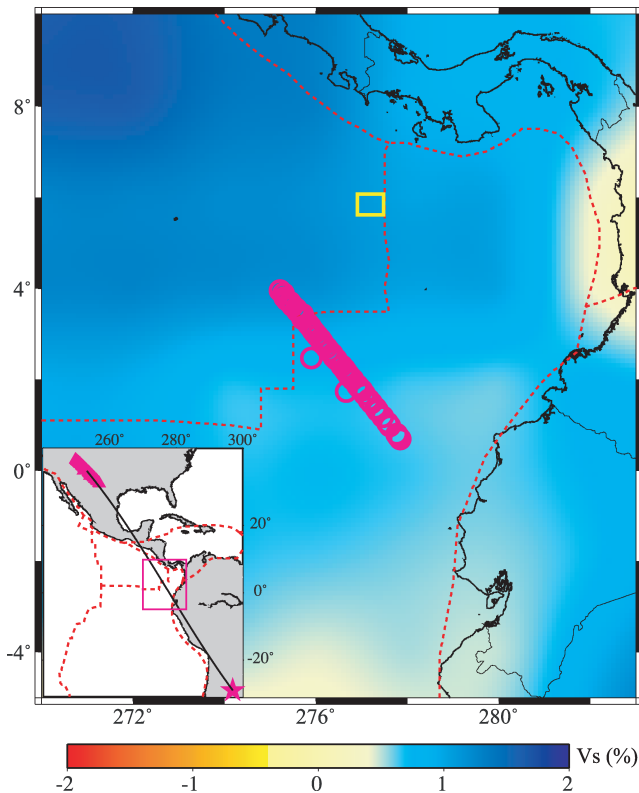


Figure 7. Map showing the reflection points at the core–mantle boundary for the seismograms recorded by the RISTRA array from the South American earthquake used in this study (purple circles). Colour shows the velocity perturbations within the D'' layer of the Grand (2002) model. Dashed red lines indicate plate boundaries. Yellow box shows the region studied by Sun *et al.* (2006). Inset shows the RISTRA array (triangles), the deep focus earthquake and a representative ray path.

D'' area in the globe (e.g. Lay *et al.* 2004; Thomas *et al.* 2004; Hutko *et al.* 2006; Sun *et al.* 2006).

Large-angle reflection from the D'' discontinuity, SdS , can be clearly seen from the raw data (Fig. 8a). Prior to the inversion, we first removed the instrument response from each seismogram, rotated the two horizontal components of the seismograms to the radial and transverse components, and then low-pass filtered the seismograms with a corner frequency of 0.2 Hz. To estimate the impulse response from the D'' layer, we further deconvolved the source time function from the transverse-component seismograms. The source time function is estimated by stacking the S phase within a time window of 4 s before and 9 s after the S arrival. An iterative deconvolution technique (Ligorria & Ammon 1999) was used in the processing. The deconvolved seismograms are shown in Fig. 8(b). They were further back propagated to 2400 km deep with the Kirchhoff integral eq. 2 (Fig. 8c). Here we used the velocity model of Grand (2002) in the back projection.

The incident angles to the D'' region of our data set are around 62° . As shown in the previous synthetic test, the resolution power to the lateral variations of seismic structure in the D'' layer decreases with increasing incident angle. Sun *et al.* (2006) found that the D'' discontinuity in this area is relatively flat, with a topographic relief of less than 10 km. We conducted a resolution test on D'' discontinuity topography with the same source–receiver geometry of the data. A simple staircase function was assumed as the input topography and was used to create synthetic seismograms for imaging (Fig. 9). With the given ray geometry, the resolvable undulations in the D'' discontinuity is between 11 and 17 km (Fig. 9). Considering these facts, our goal here is to determine a robust 1-D model. We started with the 1-D model of Grand (2002) and calculated the gradients within the 2-D model space. We then averaged the 2-D gradients at each depth to update the 1-D models. So the 1-D model obtained here can be considered as the 1-D average of the velocity structure within the study region. The final model was obtained

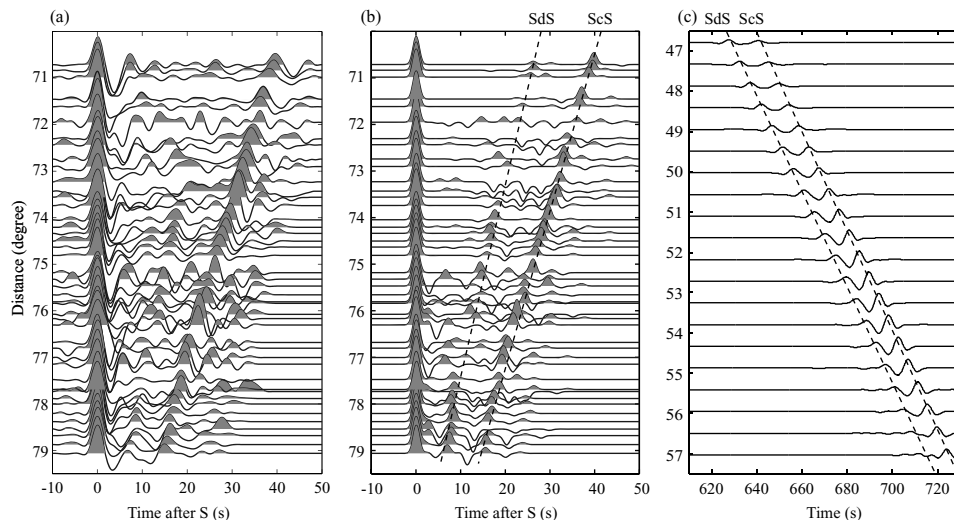


Figure 8. (a) The transverse-component seismograms recorded by the RISTRA array plotted by epicentral distance. (b) Seismograms after the deconvolution to remove the source and instrument response. Note the clear SdS arrivals between S and ScS . (c) Virtual seismograms recorded at 2400 km depth calculated from a Kirchhoff extrapolation of the surface records. Note amplitudes of ScS and SdS shown in the virtual seismograms at small and large distances could be incorrect due to an incomplete Kirchhoff integral during the back projection. Thus only the virtual seismograms at distance range $\sim 51^\circ$ to 53° were used in the inversion.

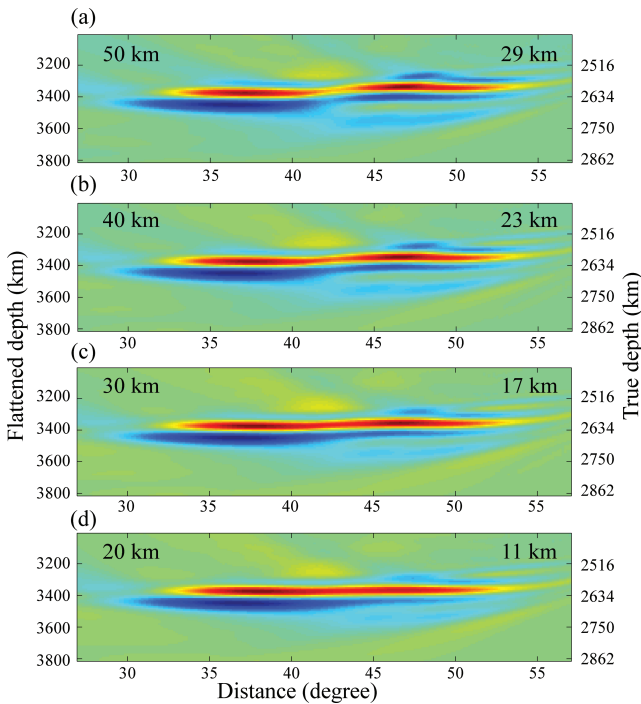


Figure 9. 2-D inversion results from four models with different D'' discontinuity topography. The same incident angle ($\sim 62^\circ$) with the real data was used in computing the synthetic seismograms. The input D'' discontinuity has a step in the model with different heights from 11 km to 29 km. The depth resolution of the D'' discontinuity with the given source–receiver geometry is between 11 and 17 km (c and d).

after 12 iterations. The updated models of the 2nd, 4th and 8th iteration are shown in Fig. 10(a). Fig. 10(b) shows the progressive reduction of the misfit between the observed data and the synthetic prediction. The misfit reaches at a minimum at the 12th iteration. As the least-square misfit function in a 1-D inversion scheme is a quadratic function, we take the velocity of this iteration as the final model. Synthetic seismograms (thin black lines) calculated from the initial and the final models are shown with the observed data (thick black lines) in Figs 10(c) and (d), respectively. Note the match between the data and the synthetics computed from the final model (Fig. 10d), which although imperfect, is considerably better than the initial model in terms of fitting the SdS phase.

6 DISCUSSION

The velocity model of Sun *et al.* (2006) is shown as dashed line in Fig. 10(a). Our final model (red line) agrees very well their model, except that our model is rather smooth, which reflect the nature of inversion. Because of the small amount of data and the low frequency content in the data, together with the fact that we were seeking for 1-D velocity structure, the resulting models thus tend to be smooth.

The S-wave velocity increase from 7.295 to 7.530 km s^{-1} , approximately a 3.2 per cent increase, over a ~ 70 km depth range. It is now generally believed the D'' discontinuity is caused by the post-perovskite phase transition (Murakami *et al.* 2004; Oganov & Ono 2004; Wookey *et al.* 2005). The calculated S-wave veloc-

ity jump associated the post-perovskite phase transition is only 1 per cent (Iitaka *et al.* 2004; Oganov & Ono 2004; Tsuchiya *et al.* 2004; Stackhouse *et al.* 2005), much less than the seismically observed velocity increase across the D'' discontinuity. It has been proposed that the observed large seismic velocity jump might be caused by the strong elastic anisotropy of the post-perovskite phase (Murakami *et al.* 2005). Another possible interpretation is that the observed high-velocity increase might be a combination effect of the post-perovskite phase transition and the high velocity structure associated with the thermal and chemical differences between the subducted slabs in the area and the background mantle.

The second feature in our model as well as in the model of Sun *et al.* (2006) is the rapid velocity decrease at the base the mantle. The velocity reduction is more than 5 per cent compared with the 1-D velocity model of Grand (2002). We believe this to be a robust feature as it appeared in the models derived from different data sets with different image techniques. Again different interpretations can be invoked for the origin of this velocity reduction. Hernlund *et al.* (2005) interpreted it to be caused by a backward transformation from post-perovskite to perovskite, and used it to constrain the thermal structure within the D'' layer as well as the heat flux from the core. There is another scenario that can also explain the lower velocity right above the CMB. Tan *et al.* (2002) found that subducted slabs can have important consequences on plume formation. While plumes tend to preferentially develop on the edge of slabs, ‘mega-plume’ can be developed beneath the subducted slabs as a consequence of long-term heating from the core. Thus the lower velocity structure observed here could reflect a thin hot layer sandwiched by the cold slab and hot core.

7 CONCLUSIONS

We developed a localized waveform inversion method for teleseismic imaging. Inversion is performed only in a localized region that requires accurate modelling while ray theory is used for wavefield extrapolation outside the study region. Synthetic tests indicate that the inversion, while being computationally efficient, can recover both large and small-scale structures in a number of input models. We applied this method to the broadband waveform data recorded by RISTRA array from a deep south American earthquake. The resulting velocity structure showed an excellent agreement with previous studies, suggesting that the hybrid waveform inversion is a feasible and an effective technique for imaging the heterogeneous D'' region.

ACKNOWLEDGMENTS

We thank the IRIS data Management Center for providing the waveform data. We also thank the Colorado Plateau/Rio Grande Rift Seismic Transect Experiment (LA RISTRA) experiment team for collecting the high quality data. Discussions with X. Cheng, M. Miller and E. Vanacore were helpful in preparing the manuscript. Critical comments from two anonymous reviewers and the Editor significantly improved the quality of this paper. This work was supported by NSF CMG grant 0620821 (YH, AL) and NSF grant EAR-0748455 (FN).

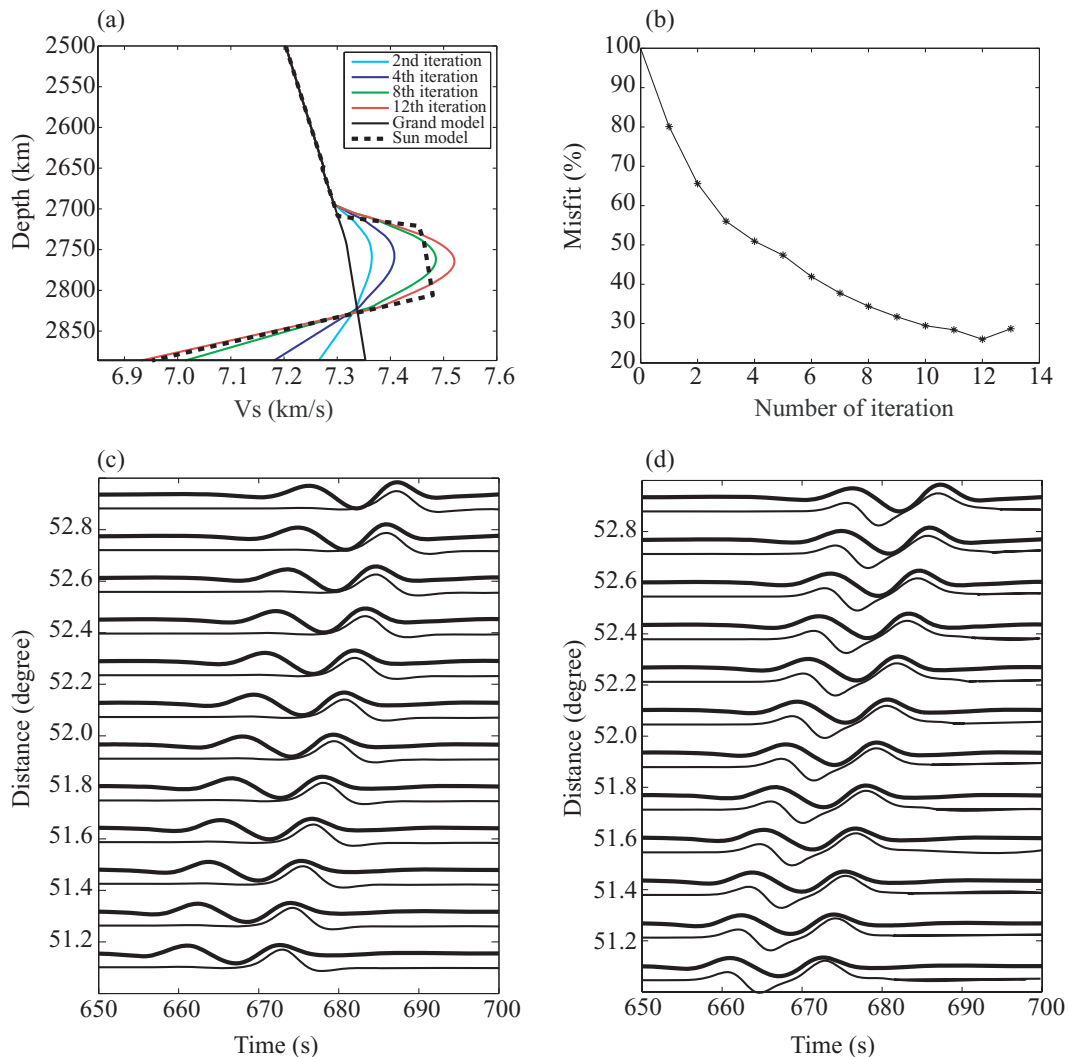


Figure 10. (a) The final velocity model (red solid line) is shown with the initial model (black solid line). The model from Sun *et al.* (2006) is shown for comparison. (b) Misfit between the data and synthetics are shown as a function of iteration number. Note the progressive improvement in the fit through the 12th iteration, which is taken as the final model. The observed seismograms are shown with the observed seismograms are shown with the synthetics calculated from the initial (c) and the final model (d). Note the *SdS* phase is now reasonably well fit in (d).

REFERENCES

- Alterman, Z. & Karal, F.C., 1968. Propagation of elastic waves in layered media by finite-difference methods, *Bull. seism. Soc. Am.*, **58**, 367–398.
- Berenger, J.P., 1994. A perfectly matched layer for the absorption of electromagnetic waves, *J. Comput. Phys.*, **114**, 185–200.
- Berkhout, A.J. & Wapenaar, C.P.A., 1988. True amplitude extrapolation of primary seismic waves I: one-way versions of the Kirchhoff integral, *Geophysics*, **54**, 460–467.
- Beylkin, G. & Burridge, R., 1990. Linearized inverse scattering problems in acoustics and elasticity, *Wave Motion*, **12**, 15–52.
- Freudenreich, Y. & Shipp, R., 2000. Full waveform inversion of seismic data: frequency versus time domain, *Lithos Sci. Report*, **2**, 25–30.
- Garnero, E.J., Grand, S.P. & Helmberger, D.V., 1993. Low P-wave velocity at the base of the mantle, *Geophys. Res. Lett.*, **20**, 1843–1846.
- Grand, S.P., 2002. Mantle shear-wave tomography and the fate of subducted slabs, *Phil. Trans. R. Soc. Lond., Ser. A*, **360**, 2475–2491.
- Hernlund, J.W., Thomas, C. & Tackley, P.J., 2005. A doubling of the post-perovskite phase boundary and structure of the Earth's lowermost mantle, *Nature*, **434**, 882–886.
- Hutko, A., Lay, T., Garnero, E.J. & Revenaugh, J., 2006. Seismic detection of folded, subducted lithosphere at the core-mantle boundary, *Nature*, **441**, 333–336.
- Iitaka, T., Hirose, K., Kawamura, K. & Murakami, M., 2004. The elasticity of the MgSiO₃ post-perovskite phase in the Earth's lowermost mantle, *Nature*, **430**, 442–445.
- Ishii, M. & Tromp, J., 1999. Normal-mode and free-air gravity constraints on lateral variations in velocity and density of the Earth's mantle, *Science*, **285**, 1231–1236.
- Kendall, J.-M. & Nangini, C., 1996. Lateral variations in D' below the Caribbean, *Geophys. Res. Lett.*, **23**, 399–402.
- Kennett, B.L.N., 1988. Systematic approximations to the seismic wavefield, in *Seismological Algorithms*, pp. 237–259, ed. Doornbos, D.J., Academic Press, San Diego.
- Kennett, B.L.N. & Engdahl, E.R., 1991. Travel times for global earthquake location and phase identification, *Geophys. J. Int.*, **105**, 429–465.
- Lay, T. & Garnero, E.J., 2004. Core-mantle boundary structures and processes, in *The State of the Planet: Frontiers and Challenges in Geophysics*, Vol. 19, pp. 25–41, eds Sparks, R.S.J. & Hawkesworth, C.J., Geophysical Monograph 150, IUGG, doi:10.1029/150GM04.

- Lay, T. & Helmberger, D.V., 1983. A lower mantle S-wave triplication and the velocity structure of D'' , *Geophys. J. R. astr. Soc.*, **75**, 799–837.
- Lay, T., Garnero, E.J. & Russell, S.A., 2004. Lateral variation of the D'' discontinuity beneath the Cocos plate, *Geophys. Res. Lett.*, **31**, L15612, doi:10.1029/2004GL020300.
- Levander, A., 1988. Fourth-order finite-difference P-SV seismograms, *Geophysics*, **53**, 1425–1436.
- Ligorria, J.P. & Ammon, C.J., 1999. Iterative deconvolution and receiver-function estimation, *Bull. seism. Soc. Am.*, **81**, 2504–2510.
- Miller, M. & Niu, F., 2008. Bulldozing the core-mantle boundary: localized seismic scatterers beneath the Caribbean Sea, *Phys. Earth planet. Inter.*, **170**, 89–94.
- Mora, P., 1987. Nonlinear two-dimensional elastic inversion of multioffset seismic data, *Geophysics*, **52**, 1211–1228.
- Mori, J. & Helmberger, D.V., 1995. Localized boundary layer below the mid-Pacific velocity anomaly identified from PcP precursor, *J. geophys. Res.*, **100**, 20 359–20 365.
- Murakami, M., Hirose, K., Sata, N., Ohishi, Y. & Kawamura, K., 2004. Phase transition of $MgSiO_3$ perovskite in the deep lower mantle, *Science*, **304**, 855–858.
- Murakami, M., Hirose, K., Sata, N. & Ohishi, Y., 2005. Post-perovskite phase transition and crystal chemistry in the pyrolitic lowermost mantle, *Geophys. Res. Lett.*, **32**, L03304, doi:10.1029/2004GL021956.
- Niu, F. & Wen, L., 2001. Strong seismic scatterers near the core-mantle boundary west of Mexico, *Geophys. Res. Lett.*, **28**, 3557–3560.
- Oganov, A.R. & Ono, S., 2004. Theoretical and experimental evidence for a post-perovskite phase of $MgSiO_3$ in Earth's D'' layer, *Nature*, **430**, 445–448.
- Pratt, R.G., Shin, C. & Hicks, G.J., 1998. Gauss-Newton and full Newton methods in frequency space seismic waveform inversion, *Geophys. J. Int.*, **133**, 341–362.
- Revenaugh, J. & Meyer, R., 1997. Seismic evidence of partial melt within a possibly ubiquitous low-velocity layer at the base of the mantle, *Science*, **277**, 670–673.
- Stackhouse, S., Brodholt, J.P., Wookey, J., Kendall, J.-M. & Price, G.D., 2005. The effect of temperature on the seismic anisotropy of the perovskite and post-perovskite polymorphs of $MgSiO_3$, *Earth planet. Sci. Lett.*, **230**, 1–10.
- Stead, R.J. & Helmberger, D.V., 1988. Numerical-analytical interfacing in two dimensions with applications to modeling NTS seismograms, *Pure appl. Geophys.*, **128**, 153–174.
- Sun, D.Y., Song, T.R.A. & Helmberger, D., 2006. Complexity of D'' in the presence of slab-debris and phase changes, *Geophys. Res. Lett.*, **33**, L12S07, doi:10.1029/2005GL025384.
- Tan, E., Gurnis, M. & Han, L.J., 2002. Slabs in the lower mantle and their modulation of plume formation, *Geochem. Geophys. Geosyst.*, **3**, 1067, doi:10.1029/2001GC000238.
- Tarantola, A., 1984. Inversion of seismic reflection data in the acoustic approximation, *Geophysics*, **49**, 1259–1266.
- Thomas, C., Garnero, E.J. & Lay, T., 2004. High-resolution imaging of lowermost mantle structure under the Cocos plate, *J. geophys. Res.*, **109**, B08307, doi:10.1029/2004JB003013.
- Thorne, M.S., Lay, T., Garnero, E.J., Jahnke, G. & Igel, H., 2007. Seismic imaging of the laterally varying D'' region beneath the Cocos Plate, *Geophys. J. Int.*, **170**, 635–648.
- Tsuchiya, T., Tsuchiya, J., Umemoto, K. & Wentzcovitch, R.M., 2004. Elasticity of post-perovskite $MgSiO_3$, *Geophys. Res. Lett.*, **31**, L14603, doi:10.1029/2004GL020278.
- van der Hilst, R.D., de Hoop, M.V., Wang, P., Shim, S.-H., Ma, P. & Tenorio, L., 2007. Seismostratigraphy and thermal structure of Earth's core-mantle boundary region, *Science*, **315**, 1813–1817.
- Vidale, J.E. & Hedlin, M., 1998. Evidence for partial melt at the core-mantle boundary north of Tonga from the strong scattering of seismic waves, *Nature*, **391**, 682–684.
- Virieux, J., 1984. SH wave propagation in heterogeneous media: velocity stress finite difference method, *Geophysics*, **49**, 1933–1957.
- Wang, P., De Hoop, M.V., Van Der Hilst, R.D., Ma, P. & Tenorio, L., 2006. Imaging of structure at and near the core-mantle boundary using a generalized radon transform: construction of image gathers, *J. geophys. Res.*, **111**, B12304, doi:10.1029/2005JB004241.
- Wapenaar, C.P.A., Peels, G.L., Budejicky, V. & Berkhout, A.J., 1989. Inverse extrapolation of primary seismic waves, *Geophysics*, **54**, 853–863.
- Wen, L., 2002. An SH hybrid method and shear velocity structures in the lowermost mantle beneath the central Pacific and South Atlantic Oceans, *J. geophys. Res.*, **107**, 2055, doi:10.1029/2001JB000499.
- Wen, L. & Helmberger, D.V., 1998. Ultra low velocity zones near the core-mantle boundary from broadband PKP precursors, *Science*, **279**, 1701–1703.
- Wen, L., Silver, P.G., James, D. & Kuehnel, R., 2001. Seismic evidence for a thermo-chemical boundary layer at the base of the Earth's mantle, *Earth planet. Sci. Lett.*, **189**, 141–153.
- Wilson, D., Aster, R., Ni, J., Grand, S., West, M., Gao, W., Baldrige, W.S. & Semken, S., 2005. Imaging the seismic structure of the crust and upper mantle beneath the Great Plains, Rio Grande Rift, and Colorado Plateau using receiver functions, *J. geophys. Res.*, **110**, B05306, doi:10.1029/2004JB003492.
- Wookey, J., Stackhouse, S., Kendall, J.-M., Brodholt, J. & Price, D., 2005. Efficacy of the post-perovskite phase as an explanation for lowermost-mantle seismic properties, *Nature*, **438**, doi:10.1038/nature04345.
- Wysession, M.E., Lay, T., Revenaugh, J., Williams, Q., Garnero, E., Jeanloz, R. & Kellogg, L.H., 1998. The D'' discontinuity and its implications, in *The Core-Mantle Boundary Region*, pp. 273–297, eds Gurnis, M., Wysession, M.E., Knittle, E. & Buffet, B.A., American Geophysical Union, Washington, DC.